Available online at www.sciencedirect.com

ScienceDirect

Acta Materialia 56 (2008) 4402–4416

Acta MATERIALIA

www.elsevier.com/locate/actamat

Tensile flow stress of ceramic particle-reinforced metal in the presence of particle cracking

R. Mueller [a,1], A. Rossoll [a,*], L. Weber [a], M.A.M. Bourke [b], D.C. Dunand [c], A. Mortensen [a]

[a] *Ecole Polytechnique Fédérale de Lausanne (EPFL), Laboratory for Mechanical Metallurgy, CH-1015 Lausanne, Switzerland*
[b] *Los Alamos National Laboratory (LANL), LANSCE-12, P.O. Box 1663, MS H805, Los Alamos, NM 87545, USA*
[c] *Northwestern University, Department of Materials Science and Engineering, Evanston, IL 60208, USA*

Received 23 October 2007; received in revised form 15 April 2008; accepted 1 May 2008

Abstract

A simplified model is proposed to quantify the effect of damage in the form of particle cracking on the elastic and plastic behaviour of particle-reinforced metal matrix composites under uniaxial tensile loading: cracked particles are simply replaced, in a mean-field model, with as much matrix. Pure aluminium reinforced with 44 vol.% alumina particles, tested in tension and unloaded at periodic plastic deformations, is analysed by neutron diffraction during each reloading elastic step, at 30%, 50%, 70% and 90% of the tensile flow stress. The data give the evolution of the elastic matrix strains in the composite and also measure the progress of internal damage by particle cracking. The test gives (i) the evolution of the the in situ matrix flow stress, and (ii) the evolution of load partitioning during elastic deformation with increasing composite damage. Predictions of the present model compare favourably with relevant results in the literature, and with results from the present neutron diffraction experiments.

Keywords: Two-phase materials; Mean-field analysis; Variational estimate; Neutron diffraction; Tensile behaviour

1. Introduction

Internal damage exerts a strong influence on the ductility of particle-reinforced metals: it decreases the rate of work hardening of the composites which, in turn, hastens the onset of tensile instability. As a consequence, the maximum tensile elongation of metal matrix composites tends to be well below that of their unreinforced matrix [1–6].

Three physical forms of microdamage can appear in particle-reinforced metals [7]: (i) interfacial debonding, which generally signals a defective material [8–10]; (ii) internal voiding in the matrix, particularly at strain concentration sites along or near the reinforcement/matrix interface [6,10–12]; and (iii) particle cracking, with cracks perpendicular to the largest elongation, i.e., perpendicular to the applied load in tension and parallel to it in compression [6,8,13–21]. This third mechanism dominates in many composites, notably in composites containing large angular (i.e., comminuted) reinforcements [2].

Experimental quantification of damage and measurements of its rate of accumulation can be achieved by several means; broadly, these are separated into two classes, namely direct and indirect methods [22]. Direct methods are ones where damage is measured by “counting” damage events within the strained material. This includes “post mortem” metallography on deformed samples [2,23–27] as well as several techniques that detect in situ damage events while the sample is strained: acoustic emission [28,29], in situ scanning electronic observation of strained sample surfaces [30–32], neutron [33] and synchrotron X-ray diffraction [34]. More recently, X-ray topography (or radiography) and microtomography techniques have also proved to be powerful methods [35–42]. Indirect

---

[*] Corresponding author. Tel.: +41 216934859; fax: +41 21 6934664.
E-mail address: andreas.rossoll@epfl.ch (A. Rossoll).

[1] Present address: Novelis Automotive, Painted & Specialities, CH-3960 Sierre, Switzerland

1359-6454/$34.00 © 2008 Acta Materialia Inc. Published by Elsevier Ltd. All rights reserved.
doi:10.1016/j.actamat.2008.05.004

methods are ones that monitor the progress of damage by the change it imparts on a chosen property of the material. Here, two main techniques are used, namely monitoring the gradual decrease caused by damage in (i) the density of the deforming material [11,43–45] or (ii) its Young's modulus [15,18,19,46–48].

Each method has its advantages and drawbacks. Direct methods give, as their name indicates, direct quantitative information on the progress of damage; however, they generally require considerable experimental effort (and sometimes can be influenced by artefacts of specimen preparation [49]). Indirect methods, in particular tracking Young's modulus using load/unload cycles during a uniaxial test, are comparatively much easier to implement; however, these require an interpretation framework by which the pertinent physical property change can be linked quantitatively to damage evolution within the material.

The importance of understanding the link between damage and the mechanical properties of multiphase materials is, therefore, twofold: it is a prerequisite to one's understanding of the influence of damage on the strength of materials, and it is also the required framework for interpreting measurements of its evolution by one of the most convenient methods, namely tracking the evolution of Young's modulus. Several authors have addressed the issue, using different approaches.

Damage in its various forms has been incorporated in shear lag [50], mean-field [51–56], finite element models [57–61], and also in models combining these approaches [62–64]. While the former two methods arrive at global properties by attributing different levels of damage to the phases and then averaging stresses and strains in each phase, finite element modelling is capable of capturing stress and strain disturbances around localized damage events. All three damage micromechanisms have now been addressed in three-dimensional finite element simulations, e.g., Refs. [57,65] for ductile matrix failure by microvoiding, Refs. [58,66,67] for fracture of the brittle reinforcements, and Refs. [52,61] for interface decohesion. The effect of the reinforcement spatial distribution on damage has also been addressed in finite element simulations, to show that clustering significantly increases the fraction of broken (spherical) particles, leading to enhanced reduction in the composite flow stress and ductility [60].

A major limitation of finite element modelling is that damage in two-phase materials such as particle-reinforced metals develops gradually, generally remaining relatively sporadic up to composite failure. This has the consequence that, to model the behaviour of the material realistically, a large number of second-phase particles must be included in the unit cell used. Multiparticle cell simulations have been conducted by some authors (e.g., by Ghosh and Moorthy using a Voronoi cell approach [68], and by Llorca and Segurado using a cubic unit cell [57,61]); however, this vastly increases the complexity of the calculation. Other authors have instead used averaging procedures, akin to mean-field approximations, to model the influence of the non-damaged composite surrounding simulated individual damage events (e.g., Refs. [64,69]); this, of course, makes the model approximate.

Compared with finite element simulations, mean-field approaches have the advantage that their implementation is far more direct, particularly if they can be reduced to explicit analytical expressions. Among the several existing mean-field approximations, the Mori–Tanaka model is generally used to simulate the influence of damage on the linear [51,52,55,70–72] or non-linear [56] monotonic flow stress of particulate reinforced metals. In particular, Zhao and Weng developed a tensorial solution for the linear elastic [55] and non-linear [56,73–77] behaviour of two-phase composites containing partially debonded inclusions, varying the inclusion shape and also accounting for the effect of the debonding angle on the elastic response of the material [72].

The goal in this contribution is to propose a relatively user-friendly framework for quantitative interpretation of tensile test data on damaging materials made of a hard and brittle inclusion phase embedded in a ductile metallic matrix, and to test this model. The most important damage mode is addressed, namely the cracking of particles, these being of a stiff elastic phase in a more compliant power-law matrix. Simplifications are made similar to those used earlier with non-damaging composites [78], building on recent developments in composite micromechanics to arrive at comparatively simple expressions predicting the composite uniaxial flow curve in the presence of damage.

Before the model is presented, however, some of its limitations must be emphasized. The approach rests on conventional mean-field approximations, necessary to account for the interaction between particles at non-dilute concentrations typical of most two-phase materials, and also to extend linear elasticity models to non-linear deformation; see Refs. [79,80]. In all rigour, this model is a non-linear elasticity model that can be used by extension to address the behaviour of plastically deforming materials, provided that loading remains monotonic. When damage appears while the material is strained, as is usually the case, loading is, however, never monotonic at a local level: portions of the non-linear matrix will change flow path, often leaving the yield surface, at least temporarily. In what follows, these effects are simply ignored, and the flow stress of a composite that has gradually accumulated internal damage is assimilated to that of a composite that initially contained the same amount of damage before it was deformed. This, of course, is an approximation, as is apparent with clarity, for example, from simulations of the (simpler) case of damaging ceramic fibre reinforced metals loaded along the fibre direction [81]. How much of a difference this makes in the present case is open to question, given the fact that, at any moment along its strain path, the composite mostly contains damage sites that have seen, since damage first appeared there, further deformation along its global loading path. Also, as will be shown below, despite their relative simplicity, resulting expressions provide satisfactory agreement when compared with experiment. Still, the assimilation made of a damaging composite to a predamaged composite may, in some cases (to be expected particularly when there is little matrix hardening), make a significant difference, a fact that the authors wish to emphasize from the onset.

The model is presented below, and its predictions are compared with results from the literature, both theoretical and experimental. Then a more in-depth comparison is given of the model with experimental data collected using neutron diffraction, which offers non-destructive in situ access to lattice spacings and hence to elastic strains within each phase of the material, at depths that far exceed those attainable using conventional X-ray sources [82]. The neutron diffraction data are gathered on a high-volume fraction Al–Al_2O_{3p} composite during tensile testing. The average stress in the matrix parallel to the tensile direction is deduced, and these experimental data are compared with the predictions of the model. Specifically, the in situ matrix plastic flow curve is calculated using tensile data from two other specimens in which the evolution of damage was measured. Next, the analysis for elastic load partitioning in the material is compared with neutron diffraction data. Finally, the resulting matrix flow stress parallel to the tensile direction is compared with that measured directly on the same material using neutron diffraction. The agreement is satisfactory in both cases, substantiating the relatively simple model proposed here.

2. Theory

A simplification of an earlier modification (cf., Ref. [44]) of a model described by Mochida et al. for cracked particles [52] is proposed. The Mochida model assimilates cracked particles to a matrix crack. Because it was found in earlier work that this assimilation of a cracked particle to a matrix crack produces an unrealistically strong decrease in composite modulus, the cracks were replaced with an equal number of flat spheroids of finite aspect ratio; the resulting model gave good agreement when compared with data for the damage evolution of high volume fraction alumina particle-reinforced aluminium [44]. Now, as these flat spheroids play only a minor role (given their low volume fraction), the greatest difference in the model between cracked and uncracked particles is, in fact, the replacement of the former with nearly as much matrix. The present contribution, therefore, takes the small extra step of simply assimilating a strongly bonded cracked particle surrounded by ductile matrix material to an equal volume of (undamaged) matrix. Inherent in this model is that only individually cracked particles are considered, not the linking-up of several particle cracks to form a macroscopic crack. In what follows, this model is designated the VCP (vanishing cracked particle) model.

2.1. Elastic VCP model

To simulate the influence of particle cracking, all cracked particles are simply replaced with an equal volume of matrix phase, making use throughout of the Mori–Tanaka approximation to compute the composite modulus from that of its (two isotropic) constituents.

Assimilating cracked particles to an equal quantity of undamaged matrix is not an intuitive approximation (it would not hold true with elongated fibres, for example); however, justifications exist. First, as already mentioned above, essentially the same assumption well matches data from an earlier study [44] (see Section 3.2). Secondly, this assumption is coherent with findings from finite element simulations of single-particle unit cells. Shen et al. [83] indeed concluded that, when the Young's modulus of the reinforcement is about three times the Young's modulus of the matrix, the stiffness of a unit cell containing a cracked cylindrical particle falls near that of one made entirely of matrix. Also, finite element calculations of stresses around cracked linear elastic isotropic spheroidal particles five times stiffer than a surrounding isotropic linear elastic matrix conducted by Cho et al. show that the matrix stress concentration remains near unity when the inclusion is spherical (see Figs. 4b and 11b of Ref. [84]). This, too, is consistent with the present assumption, as around such cracked stiff particles the stress field is then roughly the same as if the particle were replaced by matrix. Note also that this hypothesis and all calculations that follow can only be used for a composite deforming under uniaxial tension.

The Young's modulus (along the applied stress direction) of the composite containing a volume fraction V_{r2} of cracked particles is then given by

$$E_c = \frac{9K_cG_c}{G_c + 3K_c} \tag{1}$$

where

$$K_c = K_m + \frac{(1 - V_m - V_{r2})(K_r - K_m)(3K_m + 4G_m)}{3(V_m + V_{r2})(K_r - K_m) + 3K_m + 4G_m}$$

$$G_c = G_m + \frac{(1 - V_m - V_{r2})(G_r - G_m)G_m}{\beta_m(V_m + V_{r2})(G_r - G_m) + G_m} \text{ with}$$

$$\beta_m = \frac{6}{5} \cdot \frac{K_m + 2G_m}{3K_m + 4G_m}$$

where V_m and V_{r2} are, respectively, the matrix volume fraction and the volume fraction of damaged particles (the volume fraction of intact particles V_{r1} is then simply $1 - V_{r2} - V_m$). K_m, G_m, K_r and G_r are the bulk and the shear moduli of the matrix and the reinforcement, respectively.

If the reinforcing phase is perfectly rigid relative to the matrix phase, and both the matrix and the reinforcement are incompressible, Eq. (1) reduces to

$$E_c = \frac{3}{2} \cdot \frac{5 - 3V_m - 3V_{r2}}{V_m + V_{r2}} \cdot G_m \tag{2}$$

The corresponding matrix stress concentration factor B_m, defined as the ratio of the load borne by the matrix over the load borne by the composite in the elastic regime, is given in Appendix A.

2.2. Extension to non-linear behaviour

Extension of the relations defined for linear elasticity to monotonic elastoplastic matrix behaviour of the two-phase composite containing “vanishing cracked particles” is obtained using results from the variational principle of Ponte Castañeda [85], shown by Suquet [86] to be equivalent to a “modified” secant formulation. A Hollomon law is used to describe the plastic flow curve of the matrix material obeying von Mises plasticity with power-law hardening:

$$\bar{\sigma} = c \cdot \varepsilon_{\mathrm{pl}}^{n} \tag{3}$$

where $\bar{\sigma}$ is the matrix flow stress, $\varepsilon_{\mathrm{pl}}$ is the equivalent plastic strain, c is the matrix strength coefficient, and n is the matrix strain hardening exponent.

Secant modulus methods assimilate the matrix to a linear elastic material with appropriately chosen moduli at a given stage of total equivalent deformation $\varepsilon_{\mathrm{tot}}$ [87]. The secant Young’s modulus of the ductile matrix E_{ms} is given by

$$E_{\mathrm{ms}} = \frac{\sigma_{\mathrm{eq}}}{\varepsilon_{\mathrm{tot}}} = \frac{1}{\frac{1}{E_{\mathrm{m}}} + \frac{\varepsilon_{\mathrm{pl}}}{\sigma_{\mathrm{eq}}}} \tag{4}$$

where σ_{eq} is the equivalent stress. The secant bulk modulus of the matrix metal K_{ms} is equal to its linear elastic bulk modulus, as the matrix is plastically incompressible.

The secant shear modulus satisfies the usual relations for an isotropic material [88]; at the same time it is related to σ_{eq} by

$$G_{\mathrm{ms}} = \frac{3E_{\mathrm{ms}}K_{\mathrm{ms}}}{9K_{\mathrm{ms}} - E_{\mathrm{ms}}} = \frac{1}{\frac{1}{G_{\mathrm{m}}} + \frac{3}{\sigma_{\mathrm{eq}}}\left(\frac{\sigma_{\mathrm{eq}}}{c}\right)^{1/n}} \tag{5}$$

In the dual formulation of the “modified” secant modulus approach, the equivalent stress in the matrix is estimated as the volumetric average of the second-order moment of the stress field in the linear comparison material. This second-order moment is related to the overall compliance tensor $\underline{M}_{\mathrm{c}}$ by

$$\sigma_{\mathrm{eq}}^{2} = \frac{3}{V_{\mathrm{m}}}\left[\underline{\Sigma}_{\mathrm{c}} : \left(\frac{\partial \underline{M}_{\mathrm{c}}}{\partial(1/G_{\mathrm{m}})}\right)_{G_{\mathrm{m}}=G_{\mathrm{ms}}} : \underline{\Sigma}_{\mathrm{c}}\right] \tag{6}$$

where $\underline{\Sigma}_{\mathrm{c}}$ is the second-rank stress tensor applied to the composite material. Under uniaxial tensile conditions, $\underline{\Sigma}_{\mathrm{c}}$ contains only a single non-zero value Σ (in the tensile direction). Eq. (6) may then be simplified as

$$\Sigma = \sqrt{\frac{V_{\mathrm{m}}}{3a}} \cdot \sigma_{\mathrm{eq}} \tag{7}$$

where

$$a = \left[\frac{\partial(1/E_{\mathrm{c}})}{\partial(1/G_{\mathrm{m}})}\right]_{G_{\mathrm{m}}=G_{\mathrm{ms}}}.$$

Parameter a is the partial derivative of the inverse of the composite secant Young’s modulus, varying as a function of the inverse of the matrix secant shear modulus; this ratio depends on the average matrix equivalent strain.

The total axial composite strain Ξ_{tot} is deduced knowing the composite secant Young’s modulus E_{cs} obtained from Eq. (1) or Eq. (2), where G_{m} is replaced by G_{ms}

$$\Xi_{\mathrm{tot}} = \frac{\Sigma}{E_{\mathrm{cs}}} \tag{8}$$

Knowing the stress carried by the composite from Eq. (7) and deducing its overall axial strain from Eq. (8), the plastic axial strain of the two-phase material can then be calculated

$$\Xi_{\mathrm{pl}} = \frac{\Sigma}{E_{\mathrm{cs}}} - \frac{\Sigma}{E_{\mathrm{c}}} \tag{9}$$

It is shown below that it is possible to simplify the resulting expression considerably, also in the presence of damaged particles, if one makes a few reasonable assumptions.

3. Model behaviour

3.1. Predictions for model materials

The elastic constants of the matrix phase are taken, for the sake of illustration, to be characteristic of aluminium, namely $K_{\mathrm{m}} = 75$ GPa and $G_{\mathrm{m}} = 26$ GPa. Two types of finite modulus elastic inclusions are considered: (i) aluminium spheres with the same elastic parameters as the matrix (no contrast: Al–$\mathrm{Al_{el}}$); and (ii) alumina spheres with the following elastic moduli: $K_{\mathrm{r}} = 238$ GPa and $G_{\mathrm{r}} = 164$ GPa (high contrast composite of Al–$\mathrm{Al_2O_3}$). The limiting case of a material with an incompressible matrix and reinforcement, and with the inclusions perfectly rigid relative to the matrix (infinite contrast: $K_{\mathrm{m}}/G_{\mathrm{ms}} = K_{\mathrm{r}}/G_{\mathrm{r}} = G_{\mathrm{r}}/G_{\mathrm{ms}} = \infty$) is also considered.

3.1.1. Elasticity

Fig. 1 shows the results obtained with Eq. (1) for an aluminium matrix reinforced with alumina particles, as well as results obtained with Eq. (2) for the “infinite contrast” composite. Solutions for aluminium particles (i.e., “no contrast” composite) are not plotted, because they are trivial. The horizontal axis is the total volume fraction of broken particles. This value cannot exceed the total volume fraction of particles present; hence, these lines stop where V_{r2} reaches its maximum value of $(1 - V_{\mathrm{m}})$.

With increasing phase contrast, both families of curves decrease: cracking of a stiffer particle causes a higher relative reduction in composite modulus. The curves separate for differing volume fraction of particles (V_{m}), but remain fairly close to one another. This means that, for all practical purposes, the relative decrease in modulus caused by particle cracking can be taken to be independent of the total fraction of particles in the composites. The maximum difference between solutions obtained for the more realistic alumina–aluminium system with varying volume is ~6%. The relative modulus drop, and thus the Young’s modulus

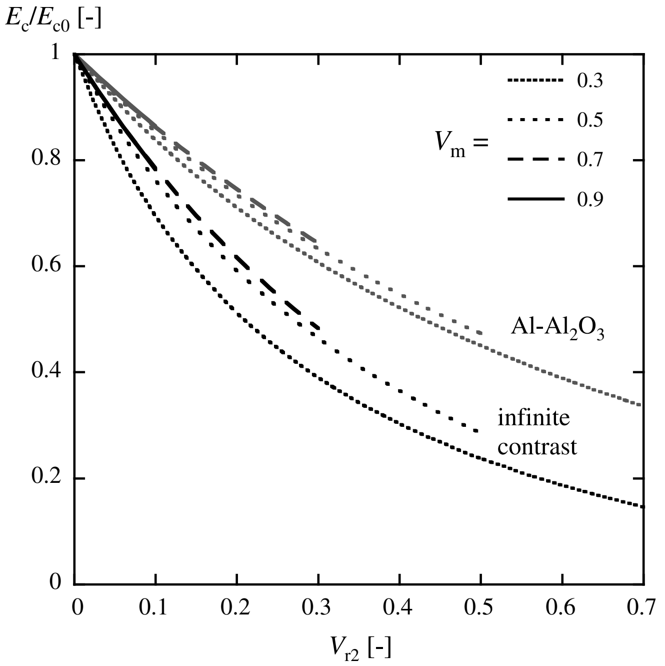

Fig. 1. Elastic response of composites with different matrix contents and phase contrasts following the VCP models. Curves for Al–Al$_2$O$_3$ are calculated using Eq. (1). Curves for "infinite contrast" composite are obtained from Eq. (2). V_{r2} is the volume fraction of damaged particles inside the material.

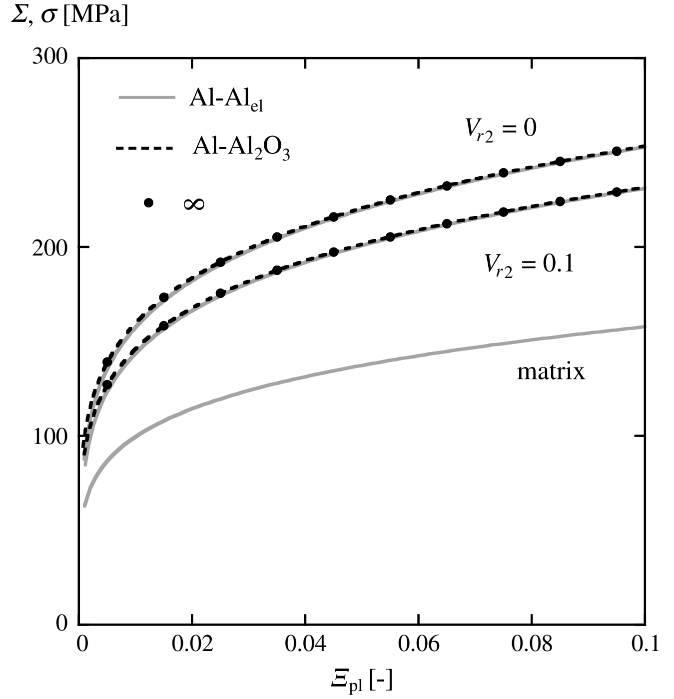

Fig. 2. Composite (power-law) plastic response for different phase contrasts and the unreinforced matrix plastic flow curve. ∞, infinite contrast composite. $c = 250$ MPa, $n = 0.2$ for all plots.

based damage parameter, $D_E = 1 - E_c/E_{c0}$ (where E_{c0} is the modulus for the intact material), then becomes a direct function of the volume fraction of cracked particles.

Note that the elastic results for the "infinite contrast" composite are shown only for completeness. If the phase contrast is finite, assuming perfectly rigid inclusions leads to an overestimation of the composite stiffness; however, Eq. (2) is useful and valid for the estimation of the overall plastic behaviour, as presented below.

3.1.2. Plasticity

Fig. 2 gives examples of tensile curves predicted for selected (realistic) material parameters, with three levels of elastic phase contrast (none; aluminium/alumina; infinite) and two levels of damage (zero or 20% of cracked particles). These curves were traced using Eq. (3) to calculate the plastic behaviour of the matrix and Eq. (9) to calculate the plastic behaviour of the composite. For Al–Al$_{el}$ and Al–Al$_2$O$_3$, E_c and E_{cs} are determined using Eq. (1). For the "infinite contrast" composite, E_c and E_{cs} are determined using Eq. (2). As can be seen, the elastic phase contrast exerts essentially no influence on the plastic behaviour of the damaged composites; this was also found for undamaged composites in Ref. [78].

3.1.3. Simplification of the relations governing the elastoplastic behaviour

Given the indifference of plastic flow stress predictions to the elastic phase contrast, Eq. (2) is hereafter used in place of Eq. (1). Moreover, in predicting the composite flow curve, elastic and plastic strain contributions are separated as in Ref. [78].

The ratio between the damaged composite flow curve and the unreinforced matrix flow curve C/c, when the matrix is incompressible and the inclusions are perfectly rigid, is given directly by Eq. (10). If the composite contains no broken particles, Eq. (10) becomes equivalent to Eq. (5.15) of Ref. [85].

$$\frac{C}{c} = \frac{\Sigma}{\sigma} = \frac{\left(\frac{5}{2} - \frac{3}{2}V_m - \frac{3}{2}V_{r2}\right)^{\frac{1+n}{2}}}{(V_m + V_{r2})^n} \tag{10}$$

where Σ and σ are, respectively, the composite and the unreinforced matrix flow curve. Note the simplicity of this equation.

Similarly to the method presented in Ref. [78]

$$\Xi_{tot} = \frac{\Sigma}{E_c} + \left(\frac{\Sigma}{C}\right)^{1/n} \tag{11}$$

is assumed, where E_c is deduced from Eq. (1), and C is given by Eq. (10). Fig. 3 confirms that there is little difference between the elastoplastic behaviour predicted by the complete variational method and by the simplified Eq. (11), as was also shown in Ref. [78].

An analytical expression is finally deduced giving the relative reduction in composite flow stress caused by internal damage (Eq. (12)), as a function of n, V_m and V_{r2}

$$\frac{\Sigma}{\Sigma_0} = \left[\frac{5 - 3V_m - 3V_{r2}}{5 - 3V_m}\right]^{\frac{1+n}{2}} \cdot \left(\frac{V_m}{V_m + V_{r2}}\right)^n \tag{12}$$

where Σ_0 is the undamaged composite flow stress.

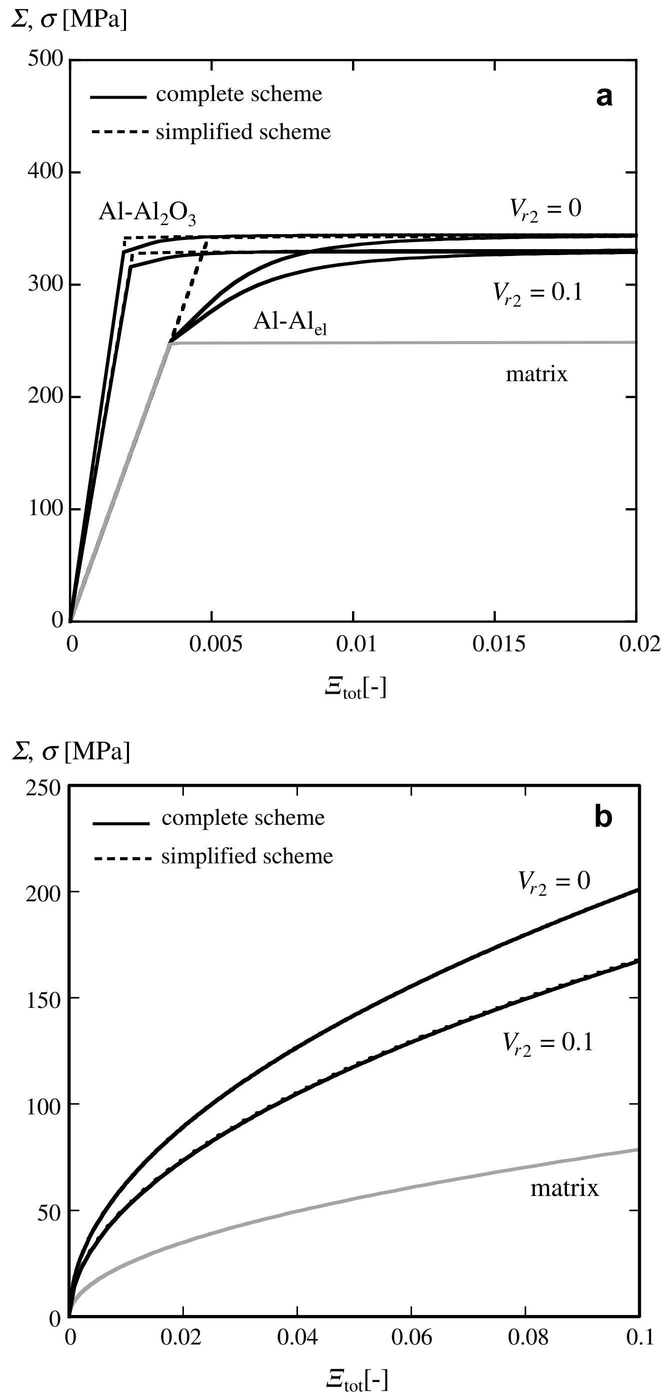

Fig. 3. VCP composite flow curves calculated with Eq. (8) via Eq. (1) (solid lines) and with the simplified scheme predictions of Eq. (12) (dashed lines). $V_r = V_{r1} + V_{r2} = 0.6$ and $c = 250$ MPa. (a) Al–Al$_{el}$, $n = 0$ and Al–Al$_2$O$_3$, $n = 0$; (b) Al–Al$_{el}$, $n = 0.5$ and Al–Al$_2$O$_3$, $n = 0.5$. In (b), the curves Al–Al$_{el}$ and Al–Al$_2$O$_3$ are superimposed.

3.2. Confrontation of analysis with data from the literature

3.2.1. Comparison with the theoretical results of Cho and Tohgo

Cho et al. [84] conducted finite element calculations of the load-carrying capacity of an isotropic linear elastic ellipsoidal inhomogeneity fractured in its mid-plane and embedded in an isotropic linear elastic matrix. Results from these calculations were then used by Tohgo and Cho [89] to propose a model describing the effect of cracking (as well as debonding) of the reinforcement on the overall composite Young's modulus. Fig. 4 shows the ratio E_c/E_{c0} for a metal matrix composite with a fraction V_r of spherical particles as calculated by the present method and by their method. Both approaches remain close to one another over all plotted values of parameters V_m and V_{r2}.

3.2.2. Comparison with finite element simulations

Segurado and Llorca [66] simulated the influence of particle fracture on the tensile behaviour of an elastoplastic matrix, using a unit cell containing seven spherical inclusions, again with parameters relevant to the aluminium/alumina system and with $n = 0.15$, $V_m = 0.85$. Their results, plotted in Fig. 8 of Ref. [66], give $\Sigma/\Sigma_0 = 0.96$ and 0.90 for $V_{r2}/V_r = 0.14$ and 0.43, respectively. Corresponding predictions of the VCP model are $\Sigma/\Sigma_0 = 0.96$ and 0.87, respectively. Comparison of the present relatively simple equations with the large unit cell simulations of Segurado and Llorca is thus quite satisfactory. Note that agreement is more erratic when present predictions are compared with results from finite element calculations based on mono-particle two-dimensional or axisymmetric unit cells [90]. The fact that such models are prone to local-

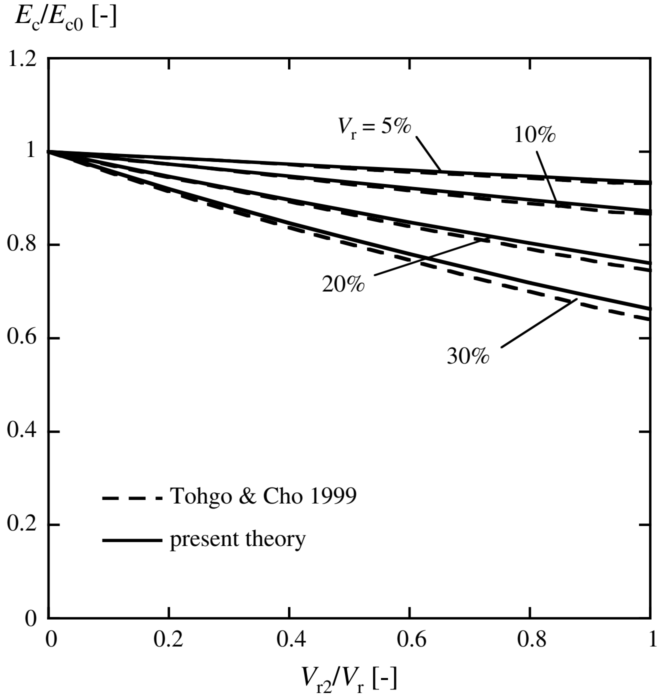

Fig. 4. Young's modulus as a function of damage evolution for composites containing 5%, 10%, 20% and 30% spherical particles. Confrontation of the present models with the damage theory of Tohgo and Cho [89].

ization of deformation in the matrix along bands that traverse the composite can be advanced as an explanation.

3.2.3. Confrontation with experimental data of Kouzeli et al.

The quantitative link between Young's modulus and the flow stress as a function of the strain was experimentally measured by Kouzeli et al. [2], defining stiffness-derived and stress-derived damage parameters, $D_E = 1 - E_c/E_{c0}$ and $D_\Sigma = 1 - \Sigma/\Sigma_0$, respectively. The former was measured using unload/reload cycles on incrementally strained (and hence damaged) composites, while the latter was assessed by measuring the flow stress during reloading after annealing of previously deformed (and hence damaged) composites. Linear regression of the experimental data plotted in Fig. 9 of Ref. [2], with lines passing through the origin leads to the conclusion that, for a composite of pure Al reinforced with a volume fraction of 47.5% Al_2O_3, D_Σ is approximately 0.7 times D_E. The present VCP model (most suited since damage occurs predominantly by particle fracture in these composites) leads to the estimation that the ratio between D_Σ and D_E is indeed relatively constant, with a value of 0.61.

The investigations of Kouzeli et al. also comprised a few metallographic estimations of the fraction of broken particles in alumina or boron carbide reinforced composites with a matrix of pure aluminium, deformed plastically and, as a result, containing cracked particles. In parallel experiments, D_E was also measured for these composites as a function of plastic strain [44]. Fig. 5 compares experimental values for D_E with predictions of the present VCP model computed from the estimated fraction of broken particles given by metallography in composites deformed to the same strain. The agreement is relatively good for the VCP model if one takes into account the difficulty in obtaining accurate measurements of the proportion of cracked particles by metallography (see estimated error bars in that figure). Also shown in Fig. 5 are the results obtained with a model developed by Zhao and Weng [55,91] for damage in the form of debonded particles, which are assimilated to anisotropic (but perfectly bonded) particles; this model is called the DP (debonded particle) model. Comparatively, predictions of D_E for the DP model are clearly too high for these (non-debonding) composites.

Confrontation of other experimental data from this study, comparing measured density-derived and modulus-derived damage parameters for these composites, with the VCP model has already been documented to give good results [44]. Indeed, the modified Mochida model used in that reference gives results essentially coincidental with the present VCP model.

3.2.4. Other data

Note that other data exist in the literature, giving metallographic assessments of the fraction of damaged particles together with measurements of the relative decrease in Young's modulus as a function of plastic strain [51,92,93]. These, however, are for composites with alloyed matrices that contain second phases other than the reinforcing particles. Therefore, additional internal damage mechanisms exist in these composites. Hence, these are not used for comparison; it is noted only that, in these composites, the measured modulus decrease often exceeds predictions of the VCP model, as is indeed expected if there is additional damage beyond particle cracking.

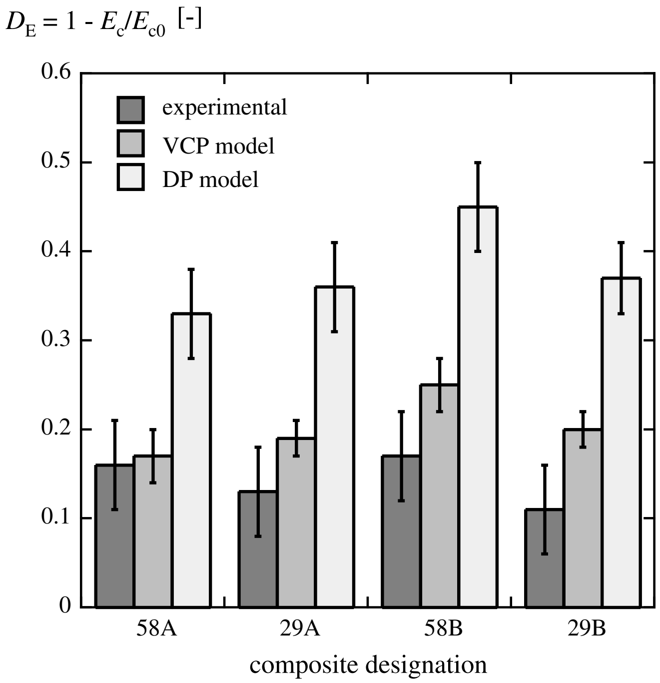

Fig. 5. Experimental and predicted Young's modulus-based damage parameter D_E, for different composites, in which the fraction of broken particles was also measured by metallography. Experimental results are from Ref. [44]. Average particle diameter = 58 or 29 in μm; A = Al_2O_3, B = B_4C particles; materials contain roughly 50% ceramic in a pure aluminium matrix. Computed results were obtained with the present VCP model as well as with the DP model [55,91].

4. Experiment

4.1. Experimental procedures

To compare the model with in situ neutron diffraction measurements, a composite of pure aluminium (99.99% Al) reinforced with 30 μm size angular alumina particles (α-Al_2O_3, from Treibacher Schleifmittel, Laufenburg, Germany) was produced by gas pressure infiltration. Detailed descriptions of the process and the composite microstructure are given elsewhere [44,94,95]. A spatially uniform distribution and a high volume fraction of the ceramic reinforcement ($V_r = 44$ vol.%) are distinctive features of the resulting material (Fig. 6). These composites yield gradually in tension from ~45 MPa, strain harden up to an ultimate tensile stress of 120 MPa at a plastic strain of 3–4%, and fracture shortly thereafter.

The Spectrometer for Materials Research at Temperature and Stress (SMARTS [96]) at the Los Alamos Neutron Science Center, NM, was used to measure in situ the matrix elastic strain on the composite subjected to uniaxial tensile loading. The sample, of dogbone shape (with $4 \times 9 \times 45\ \mathrm{mm}^3$ gauge section volume), was irradiated with a polychromatic neutron beam generated by a pulsed source. Principal beam characteristics include a continuous *d*-spacing range of 0.5–4 Å and an analysed target volume of $14 \times 4 \times 9\ \mathrm{mm}^3$. Two detector banks, situated on a plane normal to the incident beam, capture the scattered neutrons parallel and perpendicular to the tensile axis. By measuring the time of flight of the diffracted neutrons, their wavelengths can be calculated from de Broglie's relationship. Principles of neutron diffraction for strain measurement, using Bragg's law to measure the lattice spacing of several crystallographic orientations in each phase, are described in Refs. [7,82,97].

The application of the diffraction technique to measure strain and, consequently, stress partitioning is limited by the microstructural features of the observed materials. Indeed, in order to obtain a representative average value, various crystallographic planes are required. The grain size of the matrix, together with the volume fraction and size of the reinforcement particles, greatly influences the validity and precision of the results. With the present composites, the very large matrix grain size (∼1 cm) restricts observation to a limited number of usable matrix reflections. Moreover, interpretation of reflections from the alumina particles is made difficult because they break during the test, which causes a global shape change (and not just a shift) of the alumina reflection peaks. The single peak refinement method is therefore used instead of the Rietveld refinement method to analyse the data [98]. The software used is the general structure analysis system (GSAS) [99]. A sketch of the set-up is shown in Fig. 2 of Ref. [100].

In order to quantify load sharing between reinforcement and matrix during tensile testing, diffraction patterns were measured at several composite plastic deformations. Specifically, at each step of applied plastic strain, the diffraction patterns were recorded at 30%, 50%, 70% and 90% of the flow stress after eight prior unload–reload cycles (Fig. 7). This procedure was used to minimize microplasticity effects in the soft matrix, manifest as a measurable amount of stress relaxation if the sample is kept at its full flow stress during the roughly ten minutes of exposure to the neutron beam needed for diffraction data acquisition (such relaxation is not unexpected, given that the matrix consists of high-purity aluminium [101]). At zero initial plastic strain, the data were collected at five values of elastic strain: to capture the first diffraction point, the material was stressed in tension at 3 MPa, then the stress was raised to 40 MPa, with diffraction measurements recorded at every 10 MPa stress increment, without cycling. These applied stress values were selected below the offset yield point of 43 MPa ($\sigma_{0.02\%}$ in Ref. [102]), again in order to avoid transient (anelastic or viscous) effects caused by relaxation of the pure aluminium matrix.

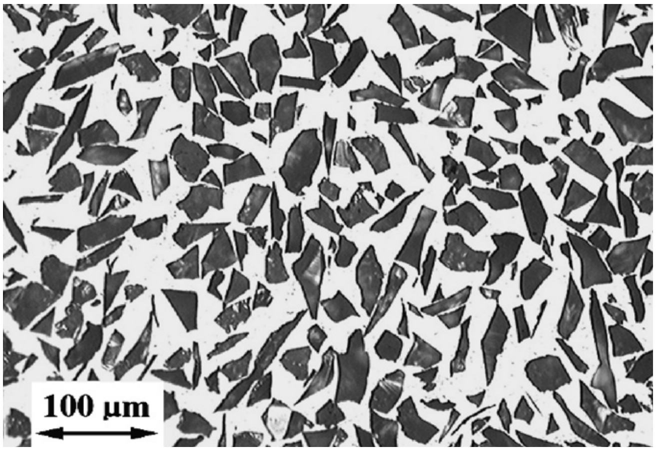

Fig. 6. Micrograph of metallographic cross-section of as-cast pure Al reinforced with 44% angular 30 μm Al_2O_3 particles.

4.2. Experimental results

The lattice spacings along a series of Al_{111} crystallographic planes, normal to the tensile axis, yielded exploitable neutron diffraction data. Parallel to the loading axis, only the Al_{200} orientation (of another grain) was exploitable. Fig. 8 shows the *d*-spacing evolution parallel (Al_{111}) and perpendicular (Al_{200}) to the loading direction as a function of applied stress, each curve corresponding to a different step of composite tensile plastic strain prior to elastic unloading–reloading cycles. As expected, in the tensile direction the *d*-spacing increases linearly as the stress increases between two levels of composite load prior to plastic deformation, with roughly the same slope (indicated by the fitted lines for the five last series of measurements) (Fig. 8a). Perpendicular to the tensile direction, the *d*-spacing decreases slightly with increasing applied stress (Fig. 8b).

Elastic phase strains in the matrix for each composite stress increment $\Delta\Sigma_A$ are deduced using Al_{111} and Al_{200} plane spacing measurements according to:

$$\Delta\varepsilon^{el}_{Al_{hkl}} = \frac{(d_{Al_{hkl}})_2 - (d_{Al_{hkl}})_1}{(d_{Al_{hkl}})_1} \tag{13}$$

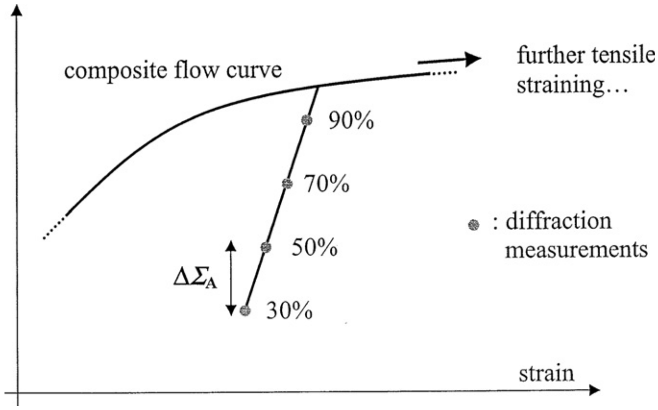

Fig. 7. Schematic description of diffraction data acquisition along stress vs strain curve of the composite at each applied tensile strain step.

with indices 1 and 2 corresponding to the lower and upper load level measurements, respectively, conducted at 30%, 50%, 70% and 90% (cf., Fig. 7). The ratio of transverse strains (cf., Fig. 8a) to longitudinal strains (cf., Fig. 8b) is ~–0.25, which is lower in absolute value than would be expected for uniaxial deformation, i.e., the (negative) value of the matrix Poisson's ratio of 0.345. Hence stresses are triaxial, notably tensile normal to the loading axis, as expected for a matrix that is reinforced with hard particles. Three increments of elastic strain $\Delta\varepsilon^{el}_{Al_{hkl}}$ are available at each step of composite plastic deformation. For each, the matrix linear elastic stress concentration factor (or stress transfer factor) B_m can be computed as

$$B_m = \frac{\Delta\sigma_1}{\Delta\Sigma_A} \tag{14}$$

where $\Delta\sigma_1$ is defined as the stress in the matrix parallel to the tensile axis. Two methods can be tested to calculate $\Delta\sigma_1$:

(i) The sampled matrix grain is assimilated to a single crystal, for which the axial strain is that corresponding to the sampled (111) reflection (Al_{111}) and stress triaxiality is ignored:

$$\Delta\sigma_1 = E_{Al_{111}} \cdot \Delta\varepsilon^{el}_{Al_{111}} \tag{15}$$

or

(ii) the matrix is supposed isotropic and the transverse strains (sampled using reflections from other matrix grains) are taken into account:

$$\Delta\sigma_1 = \frac{E_{Al} \cdot \Delta\varepsilon^{el}_{Al_{111}}}{1+\nu_{Al}} + \frac{\nu_{Al}E_{Al}(\Delta\varepsilon^{el}_{Al_{111}} + 2\Delta\varepsilon^{el}_{Al_{200}})}{(1+\nu_{Al})(1-2\nu_{Al})} \tag{16}$$

$E_{Al_{111}} = 76$ GPa, $E_{Al} = 70$ GPa and $\nu_{Al} = 0.345$ [103].

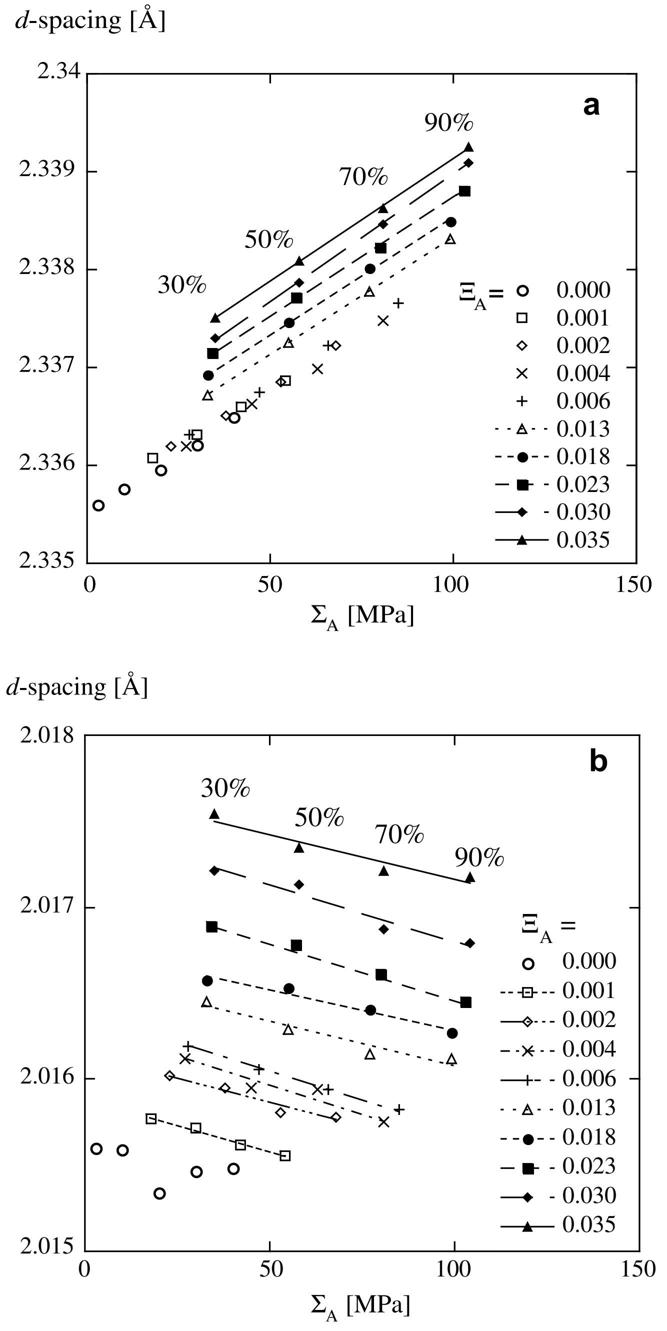

Fig. 8. d-Spacings vs applied stress for (a) Al_{111} parallel and (b) Al_{200} perpendicular to the loading direction at ten levels of composite prior tensile strain e_A given in the insert. Experimental uncertainty on d as given by the diffraction data analysis software is $\pm 4 \times 10^{-5}$ Å for Al_{111} and $\pm 7 \times 10^{-5}$ Å for Al_{200}.

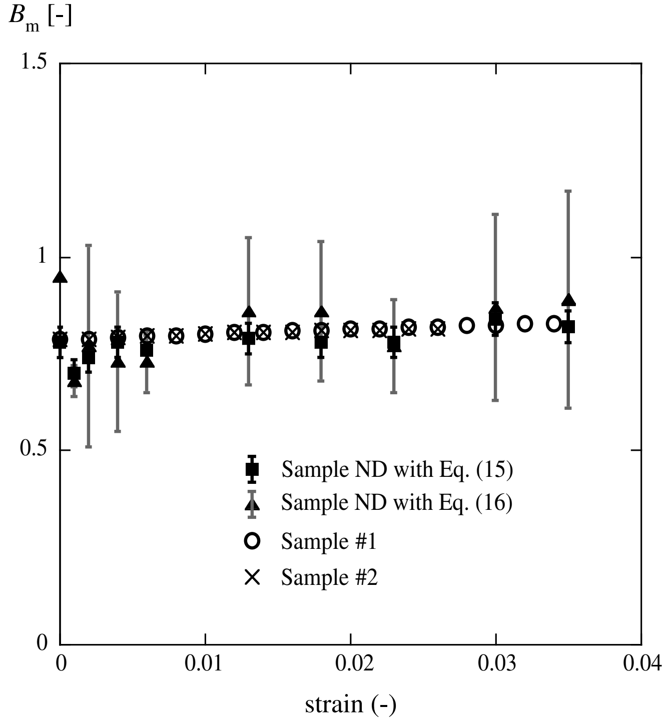

Fig. 9. Matrix elastic stress concentration factor as a function of applied tensile plastic strain. Data for Samples 1 and 2 are calculated through the present VCP model from the measured evolution with strain of the composites' Young's modulus. Experimental error on computed values of B_m for Samples 1 and 2 (due to uncertainty of the measured values of Young's modulus of ±2 GPa [44]) is ±0.01. Results for the ND sample are interpreted using Eq. (15) (squares) or Eq. (16) (triangles); experimental uncertainty on these points, reflected in plotted error bars, is estimated from the spread in raw data points in Fig. 8.

For each level of prior composite tensile deformation, values of B_m were computed for the three available elastic strain increments. Thus, for each plastic strain step, three B_m values were obtained, for which the average was then calculated (error bars are the standard deviations); this is plotted as black square and triangle points in Fig. 9. $\Delta\sigma_1$ is calculated from Eq. (15) in Fig. 9a, and from Eq. (16) in Fig. 9b. The results are similar; only the error bars are larger because of additional error associated with transverse strains.

5. Model vs experiment

In the present Al composite containing 44% vol. angular 30 μm Al_2O_3 particles, internal damage caused by tensile elongation predominantly takes the form of particle fracture, cf., Figs. 2a,b and 3a given in Ref. [44] as well as Fig. 6a given in Ref. [2]. Earlier work on those materials gives, with greater precision (because the specimen strain measurement was far more precise than in the tensile testing set-up used in neutron diffraction experiments), both the stress–strain curve of the composite and the evolution of internal damage as measured by the modulus-derived internal damage parameter D_E, defined as

$$D_E = 1 - \frac{E}{E_0} \tag{17}$$

where E is the instantaneous composite Young's modulus and E_0 is Young's modulus of the undamaged (i.e., as-processed) composite [2,15,18,19,44,46]. The stress–strain curve and the damage–strain curve are plotted in Fig. 10 for two separate samples of the same material as tested here in neutron diffraction (Samples 1 and 2 in the present work correspond to samples numbered (140)A29 and (20)A29 in Ref. [104]). Neutron diffraction results of the present work can then be compared with theory in two separate ways: one testing linear elastic deformation and the other nonlinear plastic deformation.

The data in Fig. 8, collected for the neutron diffraction (ND) sample, give access to the average stress borne by the matrix through the matrix stress concentration factor B_m (see Fig. 9). It is apparent from this figure that B_m increases weakly as composite deformation progresses. This positive slope is explained by the fact that, with increasing strain, the fraction of broken particles increases such that the fraction of stress applied to the composite that is carried by the matrix (and thus B_m) increases. These diffraction-derived data for B_m of the ND sample provide a test of linear theory, as they can be compared with values predicted by analysis of damage data for D_E of Samples 1 and 2 in Fig. 10.

A second test of data is in the non-linear plastic regime of deformation. Indeed, the extension of the model to nonlinear deformation can be used to derive the matrix in situ stress–strain curve from the composite tensile data in Fig. 10. The axial stress in the matrix can then be compared with that given directly by neutron diffraction data, by simple linear extrapolation of matrix stress values measured during reloading cycles up to the full composite flow stress. These two comparisons are made in turn below.

5.1. Matrix stress concentration factor in linear elastic deformation

The undamaged composite flow curve is approximated using a classical power-law (Hollomon) relation

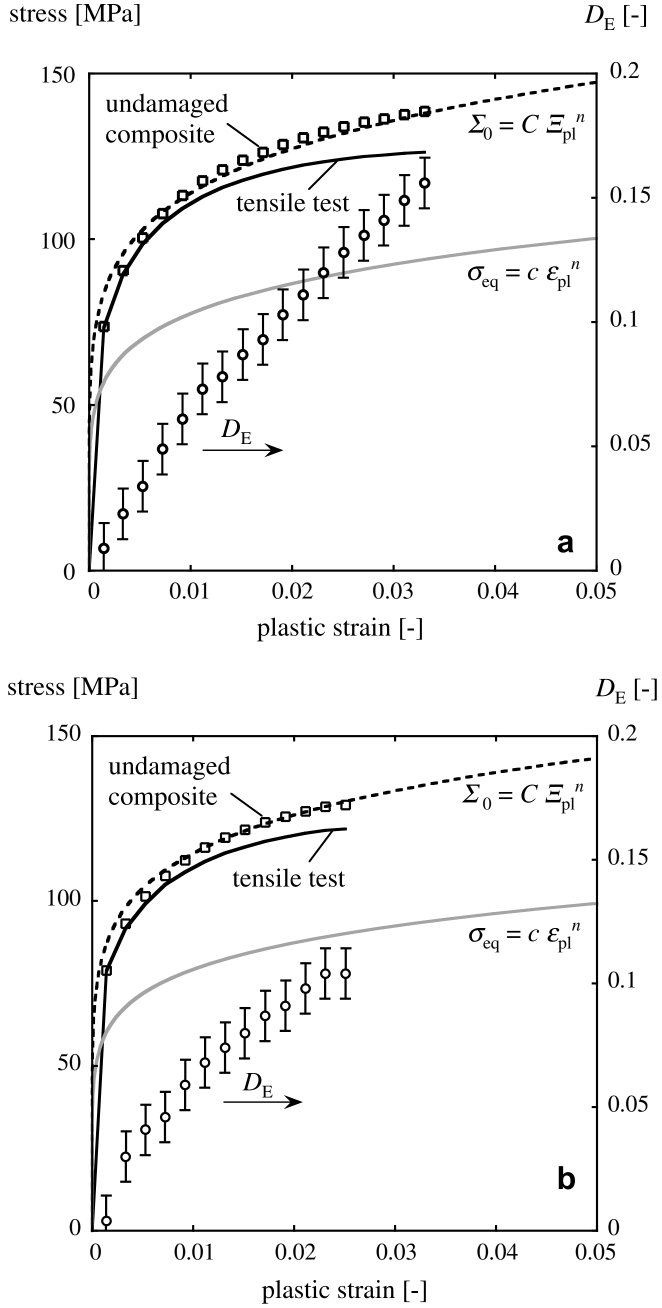

Fig. 10. Evolution of damage parameter D_E as a function of applied tensile plastic strain, and calculated in situ matrix flow stress curves: (a) Sample 1 with $V_r = 0.44$, $n = 0.16$, $a = 0.57$, $c = 164$ MPa, $C = 242$ MPa; (b) Sample 2 with $V_r = 0.44$, $n = 0.14$, $a = 0.54$, $c = 151$ MPa, $C = 218$ MPa. The error on the undamaged composite flow curve (due to the error in D_E visible on the curve) is ~ ± 1–1.5 MPa.

$$\Sigma_0 = C \cdot \Xi_{\mathrm{pl}}^{n} \tag{18}$$

where C is the undamaged composite strength coefficient, while Ξ_{pl} is the composite plastic strain.

Knowing the evolution of D_{E}, and hence of E_{c}, as a function of composite plastic strain for each of the two samples plotted in Fig. 10, the volume fraction of damaged particles V_{r2} can be calculated using the Mori–Tanaka approximation (cf., Eq. (1)). The matrix stress concentration factor B_{m} can then, in turn, be deduced; the solution is given in Eq. (A.1).

The results for Samples 1 and 2 are compared in Fig. 9 with neutron diffraction data. All the results are close to each other, substantiating the model. The apparent deviation of the neutron data points at low strain can be attributed to low applied stress (<120 MPa), to slight initial specimen misalignment, or perhaps to an influence of thermal residual stresses present after manufacturing.

5.2. Matrix in situ flow stress

The in situ matrix stress–strain curve is computed from that of the composite in two steps. First, the measured values of D_{E} are taken to deduce, using the VCP model, the stress–strain curve that the same composite would exhibit in the absence of damage. Then, this curve is fitted to a power-law and, from this undamaged (or “effective” in damage mechanics terminology [46]) composite flow curve, the matrix in situ stress–strain curve is deduced using equations given in Ref. [78].

The first step is eased considerably by the fact that the ratio α between D_{Σ}, the fractional decrease in composite flow stress caused by internal damage, and D_{E},

$$\frac{D_{\Sigma}}{D_{E}} = \alpha = \frac{1 - \left(\frac{5-3\cdot V_{\mathrm{m}}-3\cdot V_{\mathrm{r2}}}{5-3\cdot V_{\mathrm{m}}}\right)^{\frac{1+n}{2}} \cdot \left(\frac{V_{\mathrm{m}}}{V_{\mathrm{m}}+V_{\mathrm{r2}}}\right)^{n}}{1 - \frac{5-3\cdot V_{\mathrm{m}}-3\cdot V_{\mathrm{r2}}}{(5-3\cdot V_{\mathrm{m}})\cdot(V_{\mathrm{m}}+V_{\mathrm{r2}})} \cdot V_{\mathrm{m}}} \tag{19}$$

is, for all practical purposes, constant over a wide range of V_{r2}. This is shown in Fig. 11: D_{E} and D_{Σ} (calculated, respectively, via Eq. (1) and Eq. (12)) are essentially proportional for parameters relevant to the present composites.

Because the experimental tensile stress Σ applied on the composite is known, it is then straightforward to compute the flow stress at a given strain of the same composite in the undamaged condition Σ_0 [46]. Indeed, using the calculated α and the experimental evolution of D_{E} with composite strain, Σ_0 becomes

$$\Sigma_0 = \frac{\Sigma}{1 - D_{\Sigma}} = \frac{\Sigma}{1 - \alpha \cdot D_{\mathrm{E}}} \tag{20}$$

Computing the undamaged composite flow curve from the (damaging, real) composite flow curve knowing the evolution of D_{E} must be done iteratively, since the power-law exponent n of the matrix (and hence of the undamaged composite) is a priori unknown. This is easily done, however, because calculated α values not only remain nearly constant as damage accumulates, but also vary slowly with n. The relevant value of n is normally reached after one iteration using a reasonable “first-guess” estimation of the relevant α.

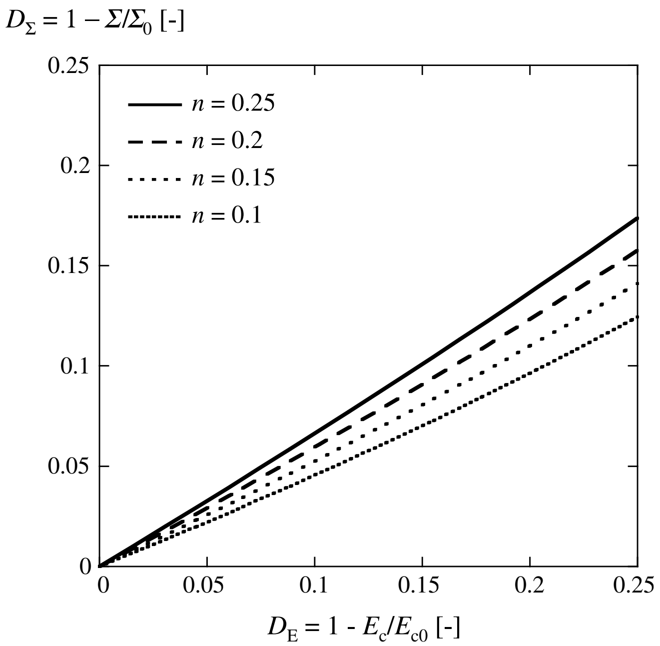

Fig. 11. Calculated relation between D_{S} and D_{E} for Al–$\mathrm{Al_2O_3}$ containing 44% of particles for four values of the work-hardening exponent n.

Fig. 12 shows, in logarithmic coordinates, the measured and corresponding undamaged composite flow curves (Σ and Σ_0, respectively, as functions of plastic composite strain) for Samples 1 and 2. Although the data nearly lie along a straight line in the double logarithmic plot, power-law hardening is not strictly obeyed: there is a slight downward curvature in the derived data points. Therefore, the work-hardening exponent of the composite varies by approximately 20%, depending on where data points are fitted. This is not unexpected, as there is no fundamental reason why the Hollomon power-law (Eq. 18), used here for convenience in mechanical analysis, should be strictly obeyed by either the composite or its matrix.

The value of n was computed by fitting a straight line through data points in the range from 1% to 3% of tensile strain, as shown in Fig. 12. This yields $n = 0.16$ and 0.14 for Samples 1 and 2, respectively. These values are reasonable for pure aluminium (e.g., Ref. [105]) and not very different from that obtained using the (more crude) estimation $D_{\Sigma} \approx D_{\mathrm{E}}$ practised in damage mechanics and used in earlier work on these composites [2,48,102,104,106].

The appropriate value of α is then calculated using the VCP model, which predicts that $\alpha = 0.57$ ($D_{\Sigma} = 0.57 D_{\mathrm{E}}$) with $V_{\mathrm{r}} = 0.44$ and $n = 0.16$, and $\alpha = 0.54$ ($D_{\Sigma} = 0.54 D_{\mathrm{E}}$) when $V_{\mathrm{r}} = 0.44$ and $n = 0.14$. The deduced undamaged composite strength coefficients C obtained from the two tests are then 242 and 218 MPa, respectively; the difference is relatively small, as can also be seen by comparing the two curves in Figs. 10 and 12.

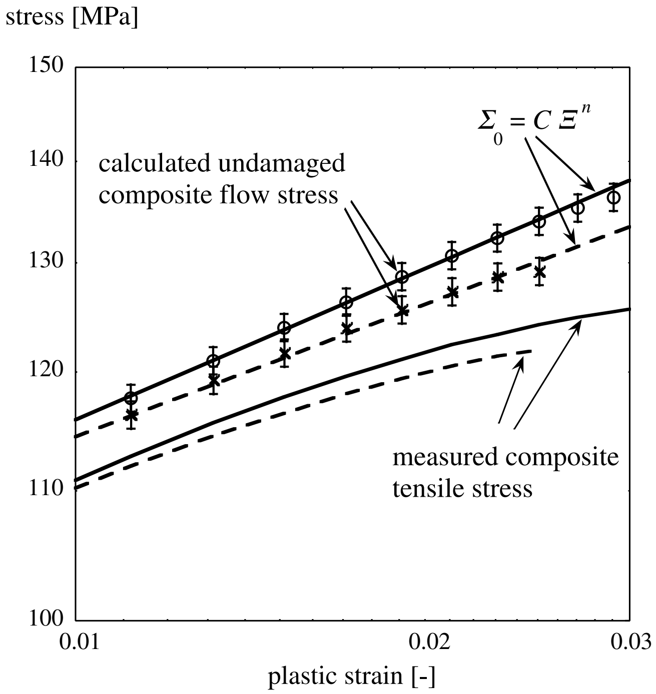

Fig. 12. Double-logarithmic plots of experimental tensile and calculated "undamaged" stress vs strain for two Al–Al$_2$O$_3$ castings, Sample 1 (continuous lines and circular data points), and Sample 2 (dashed lines and cross-shaped data points). The work-hardening exponent n (between 1% and 3% of plastic strain) and the strength coefficient C of the undamaged curves are 0.16 and 242 MPa for Sample 1, 0.14 and 218 MPa for Sample 2, respectively.

From these curves, using Eq. (28) in Ref. [78] with $V_r = 0.44$ and $C = 242$ ($n = 0.16$) or 218 MPa ($n = 0.14$), constant c of the matrix plastic flow law is deduced (Eq. (3)). This yields values $c = 164$ and 151 MPa, for the two samples, respectively.

To compute the plastic strain associated with the matrix equivalent stress σ_{eq}, it is simply noted that the ceramic particles essentially do not deform compared with the elastoplastic matrix. Also, the additional strain caused by particle fracture was measured and shown to be very small in this system [44]. The two back-calculated matrix in situ stress–strain curves are plotted in Fig. 10a and b, respectively; they agree relatively well with one another.

In the above computations, the influence of internal residual stresses of thermal origin has been neglected. Such stresses are known to exist in metal matrix composites and can influence the in situ matrix flow curve [107]. Their neglect in the present instance is justified on two grounds: (i) the matrix is of high-purity aluminium, which creeps easily at high temperature and also relaxes at room temperature; hence, residual stresses are likely to be small, and (ii) mean-field calculations of Hu and Weng [107] show that residual stresses of thermal origin exert relatively little influence on the tensile flow curve of elastic sphere reinforced metals after a relatively small strain past initial yield. Experimental data from the literature also suggest that it is legitimate to neglect internal stresses in this system. Indeed, Johannesson and Ogin [108] have shown that mean tensile thermal stresses in the matrix of similar short fibre composites are only ~10 MPa. Johannesson et al. [109] also noticed that the relaxation rate is higher in particulate composites than in fibre composites. Finally, Povirk et al. [110] as well as Fiori et al. [111] observed that thermal stresses in 2000 series Al alloy matrix composites are reduced strongly after even a relatively small amount of composite strain (0.5%), as suggested by the calculations of Hu and Weng [107].

The axial matrix stress parallel to the tensile direction σ_1 at a given value of the composite stress is $\Sigma\iota\sigma$ deduced from:

$$\sigma_1 = B_{ms} \cdot \Sigma \quad \text{with } B_{ms} = \frac{2 + V_{r1}}{2 + 3V_{r1}} \tag{21}$$

where B_{ms} is the secant matrix stress concentration factor for an incompressible matrix and a perfectly rigid reinforcement. V_{r1} is the fraction of intact particles and is deduced from Eq. (1), knowing the damage–strain curve of the two Samples 1 and 2. Fig. 13 shows the calculated axial matrix stresses as a function of the plastic tensile strain applied to the composite for Samples 1 and 2.

Neutron diffraction data can now be used to deduce the corresponding in situ matrix axial stress directly from the matrix diffraction data of the neutron diffraction sample. Because diffraction data were not taken along the tensile curve of the composite but rather during elastic unloading cycles at stresses below the composite flow stress (as explained earlier, this was done to avoid stress relaxation), the in situ matrix axial stress is deduced from the data in Fig. 8 by linear extrapolation of the lines through data collected at 30%, 50%, 70% and 90% of the composite yield stress to 100% of that value. This procedure gives the matrix stress at each point from which the composite was unloaded/reloaded along its flow curve.

The resulting data from neutron diffraction are shown in Fig. 13 as full squares (single crystalline matrix; Eq. (15)) or triangles (isotropic matrix; Eq. (16)). These are in good agreement with the matrix in situ axial stress determined as described above for Samples 1 and 2 from theory using tensile data.

The general performance of the simple model presented here for the uniaxial deformation of linear and power-law composites damaging by particle cracking is, in conclusion, quite satisfactory, especially if one takes into account its simplicity and the fact that no adjustable parameters were used in the present comparison with data. While the model is simple and relatively user friendly, it rests on assumptions and is restricted to uniaxial loading: as the composite undergoes damage during deformation, it becomes anisotropic. This is an important point not to be overlooked in extending analysis to multiaxial deformation [112,113]. Although simple extensions of the model for uniaxially loaded composites stressed along other directions than the deformation axis are fairly obvious, the model as presented here is hence not intended for multiaxial deformation.

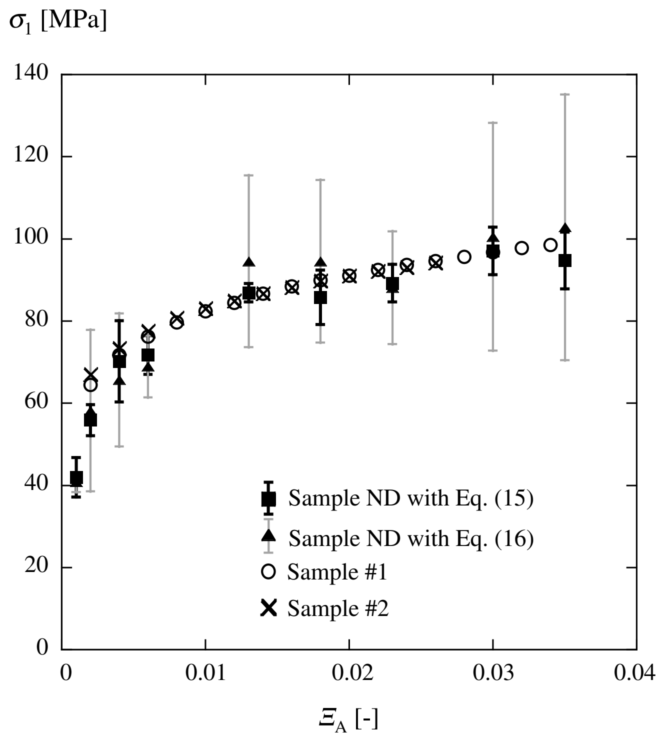

Fig. 13. In situ matrix axial stress vs applied tensile plastic strain, as predicted for Samples 1 and 2 from the measured Young's modulus evolution compared with neutron diffraction data for the ND sample, treating data alternatively using Eq. (15) or Eq. (16). The error on the computed data points (carried over from error in modulus measurement) for Samples 1 and 2 is ~ ± 1 MPa.

A second limitation is that it assumes particles of spherical shape. Particles such as those in the present composites are, in fact, angular (Fig. 6). An earlier study using metallography coupled with stereological analysis found that these particles are closer to oblate spheroids with an aspect ratio $w \approx 0.30$ than to spheres [114]. The influence of the finite aspect ratio of the present particles is, however, likely to be small, and can most likely be neglected in the calculation. Taking $w = 0.3$ and $V_r = 0.5$, the modulus increase computed with Benveniste's [115] modification of the Mori–Tanaka scheme to a random (isotropic) orientation of inclusions yields a stiffness increase of a mere 4%, as compared with spherical inclusions.

Finally, further limitations to the applicability of the model are also worth emphasizing. The model is intended, and has been checked, for materials with a uniform distribution of particulate reinforcement (no clustering) and non-localized damage. Its applicability to composites containing more than ~50% particles was also not explored. In the elastic regime, the ratio of stiffness of the reinforcement over the matrix has to be ~3–6 (as for typical MMCs, but not, for example, for Al–Si); however, this limitation does not apply to the plastic regime. And finally, the model obviously does not account for damage modes other than particle cracking (e.g., if matrix or interfacial void growth and coalescence obtain).

6. Conclusion

A simple analytical approach that incorporates the influence of internal damage by particle cracking is proposed to predict the tensile flow curve of metals reinforced with spherical particles of a hard second phase. The model simply replaces a fractured inclusion with the same volume of matrix. Relatively simple analytical expressions, namely Eq. (1) for elastic and Eq. (12) for plastic behaviour of the matrix, result. Agreement between this model and results in the literature from both experiment and finite element simulation of composites of this type is satisfactory.

The model is then compared with data obtained from neutron diffraction. Elastic unloading and reloading cycles were conducted on pure aluminium reinforced by a high volume fraction of alumina particles at different tensile plastic strain levels. Neutron diffraction data were collected during the elastic reloadings. These data are used to access (i) the stress partitioning ratio between matrix and reinforcement within the composite, and (ii) the in situ matrix axial stress during uniaxial tensile loading of the composite. Good agreement is found, both for linear elastic and non-linear deformation.

Acknowledgements

This research was supported by the Swiss National Science Foundation, Project No. 200020-107556. The authors gratefully acknowledge Ms Aude Hauert from the Laboratory of Mechanical Metallurgy at EPFL for several interesting discussions on the subject of this work.

Appendix A

$$B_m = \frac{1 + (\alpha_{r1} + \beta_{r1} - 1)V_{r1}}{[1 + (\alpha_{r1} - 1)V_{r1}][1 + (\alpha_{r1} + \beta_{r1} - 1)V_{r1}] - 2\beta_{r1}^2 V_{r1}^2} \tag{A.1}$$

where

$$\alpha_{r1} = \frac{F_1 + F_2}{F_1^2 + F_1F_2 - 2F_2^2} \quad \text{and} \quad \beta_{r1} = \frac{-F_2}{F_1^2 + F_1F_2 - 2F_2^2}$$

$$F_1 = 1 + D_1\left(\frac{3K_r + G_r}{9K_rG_r} - \frac{3K_m + G_m}{9K_mG_m}\right) + 2D_2\left(\frac{2G_r - 3K_r}{18K_rG_r} - \frac{2G_m - 3K_m}{18K_mG_m}\right)$$

$$F_2 = (D_1 + D_2)\left(\frac{2G_r - 3K_r}{18K_rG_r} - \frac{2G_m - 3K_m}{18K_mG_m}\right) + D_2\left(\frac{3K_r + G_r}{9K_rG_r} - \frac{3K_m + G_m}{9K_mG_m}\right)$$

$$D_1 = \left(1 - \frac{9K_m + 8G_m}{15K_m + 20G_m}\right)\left(K_m + \frac{4}{3}G_m\right) - 2\left(K_m - \frac{2}{3}G_m\right)\left(\frac{3K_m - 4G_m}{15K_m + 20G_m}\right)$$

$$D_2 = \left(1 - \frac{9K_m + 8G_m}{15K_m + 20G_m}\right)\left(K_m - \frac{2}{3}G_m\right) - \left(2K_m + \frac{2}{3}G_m\right)\left(\frac{3K_m - 4G_m}{15K_m + 20G_m}\right)$$

K_m, G_m, K_r, G_r are the bulk and the shear moduli of the matrix and the reinforcement respectively; V_m, V_{r1}, V_{r2} are the volume fractions of the matrix, the intact reinforcement and the broken particles.

References

[1] Brockenbrough JR, Zok FW. Acta Metall Mater 1995;43:11.
[2] Kouzeli M, Weber L, San Marchi C, Mortensen A. Acta Mater 2001;49:3699.
[3] Lewandowski JJ, Liu C, Hunt WH. Mater Sci Engng 1989;A107:241.
[4] Llorca J. Void formation in metal matrix composites. In: Clyne TW, editor. Comprehensive composite materials. Metal matrix composites, vol. 3. Oxford (UK): Pergamon; 2000. p. 91 [chapter 3.04].
[5] Llorca J, González C. J Mech Phys Sol 1998;46:1.
[6] Spowart JE, Miracle D. Mater Sci Engng 2003;A357:111.
[7] Clyne TW, Withers PJ. An introduction to metal matrix composites. Cambridge (UK): Cambridge University Press; 1993.
[8] Teng YH, Boyd JD. Composites 1994;25:906.
[9] Lewis CA, Stobbs WM, Withers PJ. Mater Sci Engng 1993;A171:1.
[10] Besterci M, Ivan J, Kovac L. Mater Sci Engng 2001;A319–321:667.
[11] Whitehouse AF, Clyne TW. Acta Metall Mater 1995;43:2107.
[12] Nutt SR, Duva JM. Scripta Metall Mater 1986;20:1055.
[13] Llorca J. J Phys IV 1993. Colloque C7 – Suppl.;
J Phys III 1793;3.
[14] Llorca J, Poza P. Mater Sci Engng 1994;A185:25.
[15] Corbin SF, Wilkinson DS. Acta Metall Mater 1994;42:1329.
[16] Shen YL, Williams JJ, Piotrowski G, Chawla N, Guo YL. Acta Mater 2001;49:3219.
[17] Lewis CA, Withers PJ. Acta Metall Mater 1995;43:3685.
[18] Vedani M, Gariboldi E. Acta Mater 1996;44:3077.
[19] Lloyd DJ. Acta Metall Mater 1991;39:59.
[20] Zhao D, Tuler FR, Lloyd DJ. Acta Metall Mater 1994;42:2525.
[21] Finot M, Shen YL, Needleman A, Suresh S. Metall Trans 1994;25A:2403.
[22] Montheillet F, Moussy F. Physique et Mécanique de l'Endommagement. Les Editions de Physique; 1986.
[23] Caceres CH, Griffiths JR. Acta Mater 1996;44:25.
[24] Madgwick A, Ungpinitpong C, Mori T, Withers PJ. Mater Sci Engng A 2003;342:201.
[25] Li M, Ghosh S, Richmond O. Acta Mater 1999;47:3515.
[26] Pandey AB, Majumdar BS, Miracle DB. Metall Mater Trans A 2000;31A:921.
[27] Ghosh S, Li M, Moorthy S, Lee K. Mater Sci Engng 1998;249:62.
[28] Mummery PM, Derby B, Scruby CB. Acta Metall Mater 1993;41:1431.
[29] Gariboldi E, Santulli C, Stivali F, Vedani M. Scripta Mater 1996;35:273.
[30] Besterci M, Ivan J, Kovac L. Mater Lett 2000;46:181.
[31] Rabiei A, Kim BN, Enoki M, Kishi T. Scripta Mater 1997;37:801.
[32] Singh PM, Lewandowski JJ. Metall Trans 1993;24A:2531.
[33] Madgwick A, Mori T, Withers PJ. Mater Sci Engng 2002;A333:232.
[34] Wanner A, Dunand DC. Metall Mater Trans A 2000;31A:2949.
[35] Mummery PM, Anderson P, Davis GR, Derby B, Elliott KC. Scripta Metall Mater 1993;29:1457.
[36] Buffière J-Y, Maire E, Cloetens P, Lormand G, Fougères R. Acta Mater 1999;47:1613.
[37] Justice I, Poza P, Martinez JL, Llorca J. Metall Trans 1996;27A:486.
[38] Babout L, Maire E, Fougeres R. Acta Mater 2004;52:2475.
[39] Babout L, Maire E, Buffière J-Y, Fougères R. Acta Mater 2001;49:2055.
[40] Buffière JY, Maire E, Verdu C, Cloetens P, Pateyron M, Peix G, et al. Mater Sci Engng 1997;A236:633.
[41] Justice I, Anderson P, Davis G, Derby B, Elliott J. Key Engng Mater 1997;127.131:945.
[42] Maire E, Owen A, Buffière J-Y, Withers PJ. Acta Mater 2001;49:153.
[43] Ratcliffe RT. Br J Appl Phys 1965;16:1193.
[44] Kouzeli M, Weber L, San Marchi C, Mortensen A. Acta Mater 2001;49:497.
[45] Gulliver GH. Metallic alloys. London: Charles Griffin & Co., Ltd.; 1922.
[46] Lemaitre J. A course on damage mechanics. Heidelberg, Germany: Springer-Verlag; 1992.
[47] Prangnell PB, Downes T, Stobbs WM, Withers PJ. Acta Metall Mater 1994;42:3437.
[48] Kouzeli M, San Marchi C, Mortensen A. Mater Sci Engng 2002;A337:264.
[49] Mummery PM, Derby B. J Mater Sci 1994;29:5615.
[50] Llorca J. Acta Metall Mater 1995;43:181.
[51] Mochida T, Taya M, Lloyd DJ. Mater Trans Jpn Inst Metals 1991;32:931.
[52] Mochida T, Taya M, Obata M. JSME Int J 1991;I-34:187.
[53] Voyiadjis GZ, Kattan PI. Int J Plasticity 1998;14:273.
[54] Wilkinson DS, Maire E, Embury JD. Mater Sci Engng A 1997;233:145.
[55] Zhao YH, Weng GJ. Int J Solids Struct 1997;34:493.
[56] Zhao YH, Weng GJ. Int J Plasticity 1996;12:781.
[57] Llorca J, Segurado J. Mater Sci Engng A 2004;365:267.
[58] Eckschlager A, Han W, Böhm HJ. Comput Mater Sci 2002;25:85.
[59] Llorca J. Acta Metall Mater 1994;42:151.
[60] Segurado J, González C, Llorca J. Acta Mater 2003;51:2003.
[61] Segurado J, Llorca J. Acta Mater 2005;53:4931.
[62] Li C, Ellyin F. Int J Solids Struct 2000;37:1389.
[63] Maire E, Wilkinson DS, Embury JD, Fougeres R. Acta Mater 1997;45:5261.
[64] González C, Llorca J. J Mech Phys Sol 2000;48:675.
[65] Tvergaard V. Acta Mater 1998;46:3637.
[66] Segurado J, Llorca J. Int J Sol Struct 2004;41:2977.
[67] Böhm HJ, Han W, Eckschlager A. Comput Model Engng Sci (CMES) 2004;5:5.
[68] Ghosh S, Moorthy S. Acta Mater 1998;46:965.
[69] Kiser MT, Zok FW, Wilkinson DS. Acta Mater 1996;44:3465.
[70] Tong W, Ravichandran G. Compos Sci Technol 1994;52:247.
[71] Zong BY, Guo XH, Derby B. Mater Sci Technol 1999;15:827.
[72] Zhao YH, Weng GJ. J Appl Mech – Trans ASME 2002;69:292.
[73] Zhao YH, Weng GJ. Int J Damage Mech 1995;4:196.
[74] Tohgo K, Chou T-W. JSME Int J Ser A 1996;39:389.
[75] Ju JW, Lee HK. Int J Sol Struct 2001;38:6307.
[76] Sun LZ, Ju JW, Liu HT. Mech Mater 2003;35:559.
[77] Sun LZ, Liu HT, Ju JW. Int J Numer Methods Engng 2003;56:2183.
[78] Mueller R, Mortensen A. Acta Mater 2006;54:2145.
[79] Suquet P. Continuum micromechanics. Wien (New York): Springer-Verlag; 1997.
[80] Ponte Castañeda P, Suquet P. Nonlinear composites. Adv Appl Mech 1998;34:171.
[81] Ohno N, Okabe S, Okabe T. Int J Sol Struct 2004;41:4263.
[82] Noyan IC, Cohen JB. Residual stress: measurement by diffraction and interpretation. New York: Springer; 1987.
[83] Shen YL, Finot M, Needleman A, Suresh S. Acta Metall Mater 1994;42:77.
[84] Cho Y-T, Tohgo K, Ishii H. Acta Mater 1997;45:4787.
[85] Ponte Castañeda P. J Mech Phys Sol 1991;39:45.
[86] Suquet PM. CR Acad Sci Paris 1995;320:563.
[87] Berveiller M, Zaoui A. J Mech Phys Sol 1979;26:325.
[88] Shames IH, Cozzarelli FA. Elastic and inelastic stress analysis. Englewood Cliffs (NJ): Prentice-Hall; 1992.

[89] Tohgo K, Cho Y-T. JSME Int J Ser A 1999;42:521.

[90] Bourgeois N. Caractérisation et Modélisation Micromécanique du Comportement et de l'Endommagement d'un Composite à Matrice Métallique: Al/SiCp. MSS-MAT, CNRS URA 850. Châtenay Malabry. France: Ecole Centrale des Arts et Manufactures; 1994.

[91] Mueller R. Tensile behaviour of discontinuous two-phase materials: influence of matrix flow stress and internal damage. Lausanne: EPFL; 2007.

[92] Lloyd DJ, Morris PL, Nehme E. Some factors influencing the ductility and properties of particulate reinforced MMCs. In: Masounave J, Hamel FG, editors. Fabrication of particulates reinforced metal composites. Materials Park (OH), Montreal: ASM International; 1990. p. 235.

[93] Zong BY, Derby B. J Mater Sci 1996;31:297.

[94] Miserez A, Mueller R, Rossoll A, Weber L, Mortensen A. Mater Sci Engng A 2004;387–389:822.

[95] Despois J-F, Mueller R, Miserez A, Weber L, Rossoll A, Mortensen A. Structural Metallic Materials by Infiltration. In: Senkov ON, Firstov SO, Miracle DB, editors. Metallic materials with high structural efficiency. Nato science series II. Mathematics, physics and chemistry, vol. 146. Dordrecht (NL), Kiev, Ukraine: Kluwer Academic Publishers; 2003. p. 379.

[96] Bourke MAM, Dunand DC, Üstündag E. Appl Phys A 2002;74:S1707.

[97] Carter DH, Bourke MAM. Acta Mater 2000;48:2885.

[98] Daymond MR, Bourke MAM, Von Dreele RB, Clausen B, Lorentzen T. J Appl Phys 1997;82:1554.

[99] Larson AC, Von Dreele RB. GSAS, general structure analysis system. Report No. LAUR-86–748. Los Alamos (NM): Los Alamos National Laboratory; 1994.

[100] Shi N, Bourke MAM, Roberts JA, Allison JE. Metall Trans 1997;28A:2741.

[101] Frost HJ, Ashby MF. Deformation mechanism maps. Oxford (UK): Pergamon Press; 1982.

[102] Kouzeli M, Mortensen A. Acta Mater 2002;50:39.

[103] Courtney TH. Mechanical behavior of materials. New York (NY): McGraw-Hill; 1990.

[104] Kouzeli M. Tensile Behaviour of aluminium reinforced with ceramic particles. Materials Department. Lausanne: Ecole Polytechnique Fédérale de Lausanne, Switzerland; 2001. p.136.

[105] Ludwigson DC. Metall Trans 1971;2:2825.

[106] Kouzeli M, Weber L, San Marchi C, Mortensen A. Acta Mater 2003;51:6493.

[107] Hu GK, Weng GJ. Mech Mater 1998;27:229.

[108] Johannesson B, Ogin SL. Acta Metall Mater 1995;43:4337.

[109] Johannesson B, Ogin SL, Surappa MK, Tsarikopoulos P, Brynjolfsson S, Thorbjornsson IÖ. Scripta Mater 2001;45:993.

[110] Povirk GL, Stout MG, Bourke M, Goldstone JA, Lawson AC, Lovato M, et al. Acta Metall Mater 1992;40:2391.

[111] Fiori F, Girardin E, Giuliani A, Lorentzen T, Pyzalla A, Rustichelli F, et al. Physica B 2000;276–278:923.

[112] Kachanov M. Int J Damage Mech 1994;3:329.

[113] Kachanov M. Int J Fracture 1999;97:1.

[114] Weber L, Dorn J, Mortensen A. Acta Mater 2003;51:3199.

[115] Benveniste Y. Mech Mater 1987;6:147.